Research Article Vol. 10, No. 3 / March 2023 / Optica 393

Pulse-to-pulse field characterization at x-ray free-electron lasers using a speckle-correlation scattering matrix

KyeoReh Lee,[1,2,*] Jun Lim,[3,5] and YongKeun Park[1,2,4,6]

[1]Department of Physics, Korea Advanced Institute of Science and Technology, Daejeon 34141, Republic of Korea
[2]KAIST Institute for Health Science and Technology, Korea Advanced Institute of Science and Technology, Daejeon 34141, Republic of Korea
[3]Pohang Accelerator Laboratory, Pohang University of Science and Technology, Pohang, Kyungbuk 37637, Republic of Korea
[4]Tomocube Inc., Daejeon 34051, Republic of Korea
[5]e-mail: limjun@postech.ac.kr
[6]e-mail: yk.park@kaist.ac.kr
*kyeo@kaist.ac.kr

Received 19 December 2022; revised 21 February 2023; accepted 21 February 2023; published 8 March 2023

In coherent diffraction experiments, knowledge of the incident field is important to extract pure sample-induced data from measured diffraction patterns. However, this becomes challenging in x-ray free-electron lasers (XFELs), as incident fields vary from pulse to pulse due to the stochastic nature of self-amplified stimulated emission. Despite various proposed field retrieval methods, single-shot characterization of each pulse remains elusive. To address this, we propose the speckle-correlation scattering matrix as a solution. Our method directly reconstructs the complex field without sample constraints or multiple acquisitions by introducing a designed diffuser before the detector. We demonstrate the robustness of our approach through successful field reconstructions in various experimental configurations. Based on the retrieved field results, pulse-to-pulse variations in pulse intensity, position, illumination angle, and shape were analyzed. We believe our method can readily serve as an on-field and real-time pulse diagnostic tool at XFELs and improve the overall quality of all experiments performed at XFELs. © 2023 Optica Publishing Group under the terms of the Optica Open Access Publishing Agreement

https://doi.org/10.1364/OPTICA.483836

1. INTRODUCTION

Incident field characterization is important in most imaging systems, as it is closely related to achievable image quality [1], spatial resolution [2,3], and sample information [4,5]. Coherent diffractive imaging (CDI) is no exception. Rather, the significance becomes greater in CDI because the incident field (or probe) cannot be independently acquired by measuring the "background" signal without samples. Therefore, various probe decoupling strategies have been introduced, including the known-probe assumption [6,7], pre-calibration of probes [8], and simultaneous reconstruction of probes and objects based on scanning measurements [9,10], to retrieve the correct object image from diffraction patterns. The last strategy is called ptychography and is one of the most popular probe characterization techniques at synchrotron sources [8,11–14].

Single-particle imaging (SPI) is a type of CDI, but exploits femtosecond x-ray pulses generated by an x-ray free-electron laser (XFEL) to overcome the radiation damage limit of biomaterials [15–18]. By introducing the "diffraction before destruction" scheme, the incident x-ray photon flux may be the only remaining theoretical constraint that bounds the spatial resolution of SPI [19]. Therefore, the size and quality of the x-ray focus become the major parameters governing the overall quality of SPI. Subsequently, the demand for focus diagnosis routines for XFELs grows [20–22].

However, the field characterization in XFELs is more challenging than in synchrotron sources. XFELs suffer from intrinsic pulse-to-pulse fluctuations in pulse intensity, position, and wavefront due to the stochastic nature of self-amplified stimulated emission (SASE) [23]. This instability hinders the direct application of ptychography that originally assumes a stable incident field. Although several ptychographic efforts have successfully addressed the position and wavefront fluctuations [22,24–26], the need for multiple acquisitions (or sufficient oversampling) is still a challenge to on-field and real-time focus diagnosis of SASE pulses.

Various single-shot field characterization methods have been introduced for XFELs based on a Hartmann sensor [27], grating-based shearing interferometry [20,21,28,29], and speckle tracking [21,30]. These single-shot methods are primarily based on local phase gradient measurements followed by two-dimensional integration, which is useful for partially coherent illuminations [31,32]. Nonetheless, due to the integration process, they are often vulnerable to local phase ambiguities (at low-intensity points), slowly varying phases (in small shearing cases), singularities on inverse filters (in large shearing cases) [33,34], and integration

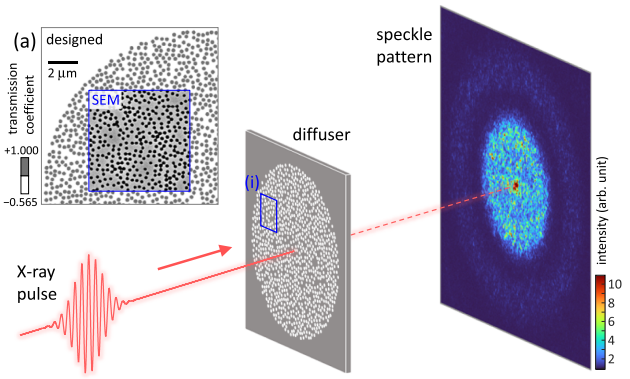

Fig. 1. Field characterization setup. A designed x-ray diffuser is placed to generate a speckle pattern on a detection plane. Appropriate spacing (200 mm) is required for the detector to resolve speckle grains. (a) The diffuser is composed of 300-nm holes located in pseudorandom positions within the diffuser with a diameter of 25 μm. A scanning electron microscopy (SEM) image of the fabricated diffuser is overlaid on the diffuser design. The transmission coefficient of a tungsten part is designed to be a negative real value (−0.565) to maximize the diffraction efficiency of the diffuser.

path dependency (due to phase residues) [35,36]. As such vulnerabilities decrease their versatility, the single-shot methods have been of limited use in slightly misaligned or aberrated situations [21,27,30].

In this study, we propose a versatile single-shot field characterization method using a speckle-correlation scattering matrix (SSM). SSM is a recently proposed field retrieval method that extracts the complex-valued incident field information from an intensity speckle pattern by exploiting the pseudorandom statistical property of the speckle [37]. To utilize the SSM, we transform arbitrary incident fields into speckle patterns by placing a designed x-ray diffuser before a detector, as shown in Fig. 1. Successful pulse characterizations are demonstrated in various experimental configurations at the Pohang Accelerator Laboratory XFEL (PAL-XFEL).

2. PRINCIPLE

A. Designed X-Ray Diffuser

The designed diffuser concept is akin to a disorder-engineered metasurface [38] in fluorescence imaging, a geometric phase diffuser in optical microscopy [39], and a modulator in coherent x-ray modulation imaging (CMI) [40].

The x-ray diffuser is made of a tungsten layer on a silicon nitride substrate. The diffuser is composed of pseudorandomly located etched holes within the diffuser diameter (25 μm), as shown in Fig. 1(a). The psudorandom hole positions were generated by the numerical free diffusion of holes within the boundary. The hole diameter (300 nm) and the minimum hole-to-hole distance (30 nm) are determined regarding the fabrication reproducibility of the manufacturer (ZonePlates Ltd., UK). The number of holes (2507) and thickness of the tungsten layer (1100 nm) were determined by maximizing the diffraction efficiency of the diffuser for a given x ray (5.456 keV). The transmission coefficient of the tungsten area was designed to −0.565, which is equal to 32% ($= 0.565^2$) transmittance with the π phase delay [Fig. 1(a)]. The fabricated hole diameters and positions were confirmed by the lobe sizes and speckle shapes of observed diffraction patterns, respectively (Fig. 1). Details of the diffuser design are in Supplement 1.

We calculated the transmission matrix (TM) from the known hole size, hole positions, and propagation length after the diffuser. Potential experimental errors in the diffuser roll angle and propagation length (200 mm) were numerically fine-tuned by maximizing the field retrieval fidelity. It is worth noting that the incident field cannot be directly retrieved from the known TM because of the phase loss during speckle pattern acquisition. This should not be confused with spatially incoherent systems having a positive and real-valued TM [41,42].

B. Speckle-Correlation Scattering Matrix

The SSM is a matrix calculated from an intensity image and the TM of the optical system. Because the principle of SSM is profoundly discussed in previous research [37,39,43] and a review [44], we will not go through all the detailed equations here. Instead, we introduce two main ideas of the SSM: oversampling and pseudorandomness.

At least two (real and imaginary) independent measurements are required to acquire a complex-valued variable. This is called oversampling, and is the fundamental principle of most field retrieval methods [45,46]. Increasing the degree of oversampling (i.e., oversampling ratio) is generally beneficial for phase problems, as it provides more evidence for a solution, thereby improving the robustness of iterative field retrieval algorithms [46–48]. If the oversampling is large enough, there could be a unique solution that satisfies all measurements simultaneously [45,49].

In the SSM method, oversampling is introduced by a diffuser, as shown in Fig. 1. The diffuser generates numerous speckle grains on the detector plane and inflates the number of acquirable independent sampling points. In terms of oversampling, this is identical to ptychography, while the diffuser is introduced here as an oversampling solution instead of sample scanning. Therefore, the iterative field retrieval algorithms used in diffractive imaging can also be applied here as demonstrated in CMI [40].

However, even though the uniqueness of the solution may be ensured by the oversampling, it does not directly mean the convergence of iterative algorithms to the solution. This is important in phase problems that are generally known to be non-deterministic polynomial-time (NP)-hard [50]. Global convergence of field retrieval would largely depend on the landscape of the loss function, initial point, and used algorithms because their loss functions are nonlinear and nonconvex and have many stationary points. This is the origin of sample-dependent phase retrieval feasibility in CDI [49], CMI [51], and even ptychography [10].

The innovation of SSM is that it provides direct and non-iterative access to the global solution by exploiting the pseudorandomness of speckle patterns [37]. The SSM can be interpreted as the coherency matrix of incident field through the Wick's (or Isserlis') theorem of Gaussian random vectors [43]. The solution is retrieved by taking the eigenvector of SSM that gives the largest eigenvalue. An additional iterative algorithm is usually required to minimize errors, as the fidelity of SSM also relates to the oversampling ratio and practical noise level.

Our field retrieval method is shown in Fig. 2. It proceeds in the following order: (i) speckle pattern measurement [Fig. 2(a)]; (ii) SSM calculation from the measured image [Fig. 2(b)]; (iii) initial guess estimation from the eigen-decomposition of SSM

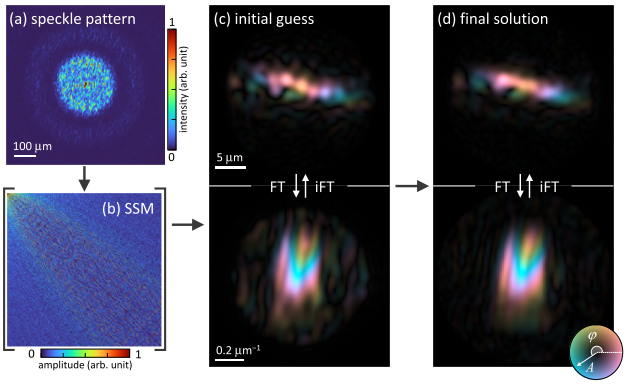

Fig. 2. Field retrieval sequence. (a) A speckle pattern is measured experimentally. (b) The speckle-correlation scattering matrix (SSM) is calculated from the speckle pattern and the transmission matrix (TM) of optical system. The SSM is an $N-$ by $-N$ Hermitian matrix, where N is the number of reconstruction modes [Eq. (S15)]. (c) The initial guess is retrieved from the eigen-decomposition of SSM. (d) The final solution is converged from the initial guess via an iterative algorithm. (c), (d) The field results are shown in both real (above) and reciprocal (below) spaces. FT and iFT are the Fourier and inverse Fourier transforms, respectively. The lightness and hue signify the amplitude (A) and phase (φ) of retrieved fields, respectively.

[Fig. 2(c)]; and (iv) convergences to the nearest solution from the initial guess through the amplitude flow [Fig. 2(d)] [48]. A detailed description of the field reconstruction sequence is in Supplement 1. Detailed principles and equations are described in a recent work with visible light that shares the identical field reconstruction flow [39].

3. RESULTS AND DISCUSSION

A. Experimental Configurations

We demonstrated our idea in various setups at both experimental hutches of hard x-ray beamlines (EH1 and EH2) of PAL-XFEL to prove its versatility, as shown in Fig. 3. The x-ray pulses with photon energy centered at 5.456 keV were generated from the undulator hall (UH) throughout the experiments. First, we utilized the Kirkpatrick–Baez (KB) mirror system in EH2 as a focusing optics, as shown in Fig. 3(a). The vertical and horizontal focusing mirrors (VFM and HFM) have focal lengths of 5.995 and 5.365 m, respectively [52]. Subsequently, we utilized a compound refractive lens (CRL) in EH1 as a focusing optics, as shown in Fig. 3(b). The CRL consists of four beryllium lenses providing an effective focal length of 8.2 m. Finally, we bypassed the offset mirrors in the optical hutch (OH) and used a double-crystal monochromator (DCM) to investigate the chromatic effect of the CRL, as shown in Fig. 3(c). The detailed distances between the optical components are provided in Fig. 3.

Based on the three setups in Fig. 3, we characterized the x-ray pulses in seven different configurations, as summarized in Table 1. Configurations KB_0, CRL_0, and mCRL represent the normal condition of the setups of Figs. 3(a), 3(b), and 3(c), respectively. Other configurations are abnormal conditions in which misalignment (KB_1, KB_2, and KB_3), aberration (KB_2 and CRL_1), or additional filtering (KB_3) were introduced. An adequate thickness of attenuators (silicon or aluminum) was used to prevent radiation damage to the diffuser, as presented in Table 1.

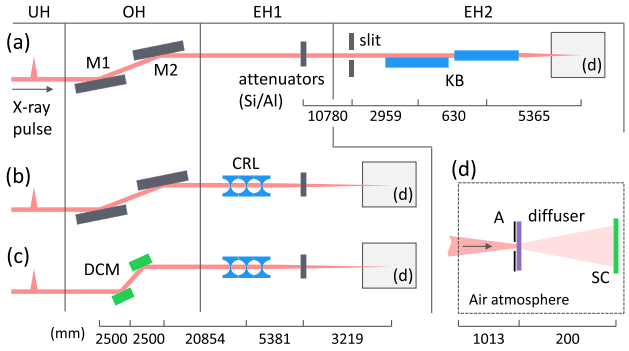

Fig. 3. Experimental setups. (a) The KB mirror system in EH2 was used as a focusing optics. (b) The CRL in EH1 was used as a focusing optics. (c) The DCM in OH was used instead of the offset mirrors (M1 and M2), while the CRL in EH1 was used as a focusing optics. (d) Diffuser-based field characterization unit. UH, undulator hall; OH, optical hutch; EH1, EH2, experimental hutches 1 and 2, respectively; M1, M2, offset mirrors 1 and 2, respectively; KB, Kirkpatrick–Baez mirror system; CRL, compound refractive lens; DCM, double-crystal monochromator; A, aperture; SC, scintillator. Distances between optical components are shown below the millimeter unit.

Table 1. Characteristics of Experimental Configurations

Identifier	Setup (Fig. 3)	Attenuator	$\Delta E/E$	Remarks
KB_0	a	Si 100 μm	0.3%	Normal condition
KB_1	a	Si 50 μm	0.3%	Not aligned KB
KB_2	a	Al 53 μm	0.3%	Aberrated, not aligned KB
KB_3	a	Si 50 μm	0.3%	Reduced slit, not aligned KB
CRL_0	b	Si 50 μm	0.3%	Normal condition
CRL_1	b	Al 45 μm	0.3%	Aberrated
mCRL	c	No attenuator	<0.01%	Normal condition

Pink beams ($\Delta E/E = 0.3\%$, Fig. S3) were used throughout the experiments except for the mCRL configuration, which utilizes a monochromatic beam ($\Delta E/E < 0.01\%$). Despite the difference in spectral bandwidths, both pink and monochromatic beams can be considered as single-frequency in our measurements, because their spectral bandwidths are much narrower than the spectral resolution of the used diffuser ($\Delta E/E = 5\%$; see Supplement 1 for details). Potential pulse-to-pulse peak frequency fluctuations would not affect the measurements similarly.

In every configuration, the diffuser-based field characterization unit is installed near the focal plane [Fig. 3(d)]. The unit is composed of an aperture, a diffuser, and an image sensor. The aperture blocks the x rays reaching outside the diffuser. It is made of a gold film with a thickness of 50 μm, and has the same diameter as that of the diffuser (25 μm). The aperture is an optional component if the pulse does not exceed the diffuser diameter, but we found that it significantly enhances the robustness of the system especially in misaligned or aberrated situations. The used image sensor is a Tb:LSO ($Tb^{3+}:Lu_2SiO_5$) scintillator equipped with an optical microscope (×10) and an sCMOS camera (6.5 μm, C11440-22C, Hamamatsu Photonics K.K.). The effective pixel size is 650 nm, while the finest speckle grain size is 2.2 μm based on the aperture diameter and diffuser–scintillator distance (200 mm). The camera

shutter was synchronized to the pulse generation triggers (10 Hz) to ensure the acquired image was generated from a single pulse.

We found that the radiation damage of a diffuser could be a practical issue. In this study, we mitigated the issue by introducing additional attenuators and preparing 100 identical diffusers on the same substrate. The diffuser was replaced in cases of radiation damage. However, for a longer durability, placing the diffuser off the focal plane is recommended, requiring a diffuser with a large diameter. We expect that the semi-permanent use of a diffuser is also possible if the diffuser could be made of radiation-damage-resistant materials, such as diamond [53,54]

B. Pulse Characterization Results

The measured speckle patterns are shown in the first row of Fig. 4. From the intensity fraction of the unmodulated term at the center, the diffraction efficiency of the used diffuser was estimated to be >90% as intended from the diffuser design. We excluded the remaining unmodulated term in the field retrieval sequences by introducing a 62.5-μm-diameter numerical beam stop. Notably, a lower signal is observed in KB_0 and KB_3 configurations. In the KB_0 configuration, due to the tighter focus, a thicker (100 μm) silicon attenuator was required to prevent diffuser damage. In the KB_3 configuration, the low fluence resulted from the reduced slit size.

The corresponding field retrieval results in real and reciprocal (or Fourier) spaces are shown in the second and third rows of Fig. 4, respectively. First, we brought the retrieved fields to the focal plane by numerical propagation, which is equivalent to quadratic phase compensation in reciprocal space, to compare the results in the same condition. Subsequently, the linear phase ramps in both real and reciprocal spaces are removed, which is also equivalent to beam centering in reciprocal and real spaces. The single field retrieval operation took 4 to 5 s using MATLAB software with a single GPU (GeForce RTX 3090, NVIDIA Corp.).

In the KB_0 configuration [Fig. 3(a)], we observe a tight focus having FWHMs of 1.24 and 1.55 μm for horizontal and vertical directions, respectively. Measured values are smaller than the previously reported values at PAL-XFEL, which are 1.94 and 2.08 μm for horizontal and vertical directions, respectively [52]. The previous wire-scanned values may have been overestimated from the practical roughness of the wire and the pulse-to-pulse position fluctuation. Slight imperfection on the VFM alignment is found from the non-uniform phase along the vertical direction in reciprocal space.

In the CRL_0 configuration [Fig. 3(b)], we observe an asymmetric focus. The retrieved focus shows FWHMs of 5.90 and 2.73 μm along horizontal and vertical directions, respectively. The size in reciprocal space (i.e., spatial bandwidth) is smaller than that of the KB mirror system, indicating the smaller numerical aperture (NA).

In the mCRL configuration [Fig. 3(c)], we observe a more symmetric focus than in the CRL_0 configuration. The retrieved focus shows FWHMs of 2.92 and 3.23 μm along horizontal and vertical directions, respectively. By comparing CRL_0 to mCRL, we infer that the asymmetric focus in the CRL_0 configuration can be derived from slight misalignment on the horizontal position of CRL. Due to the chromatic property of CRL, the positional offset induces a prism-like spectroscopic effect and elongates the focus along the offset direction for pink beams.

The KB_1 configuration is based on KB_0, but before the fine alignment of the KB mirror system. We observe significant deteriorations in the size, shape, and wavefront of the focus. From the clear aperture reduction and strong phase variation along the horizontal direction in reciprocal space, we infer that the non-mirror surface of HFM is applied.

KB_2 and CRL_1 configurations are based on KB_1 and CRL_0, respectively, but aluminum foil was introduced as an attenuator instead of silicon. Because of the uneven surface of the aluminum foil, significant aberration was introduced, and it can be observed as the phase variation in reciprocal space. These results demonstrate the robustness of our method even for complex-shaped incident fields.

Although the KB_3 configuration is based on KB_1, the slits before the KB mirror system are reduced. The reduced slits can directly be observed as a rectangular aperture in reciprocal space. The phase values within the rectangular window are mostly preserved. This result agrees well with the expectation and demonstrates the fidelity of our field characterization method.

C. Spatial Resolution

Compared to the reconstruction field of view (FOV), which is a constant determined by the diffuser diameter (25 μm), the reconstruction bandwidth (B) is a tunable variable determined by the numerically generated TM [39]. Nonetheless, B cannot be set indefinitely large to secure a sufficient oversampling ratio.

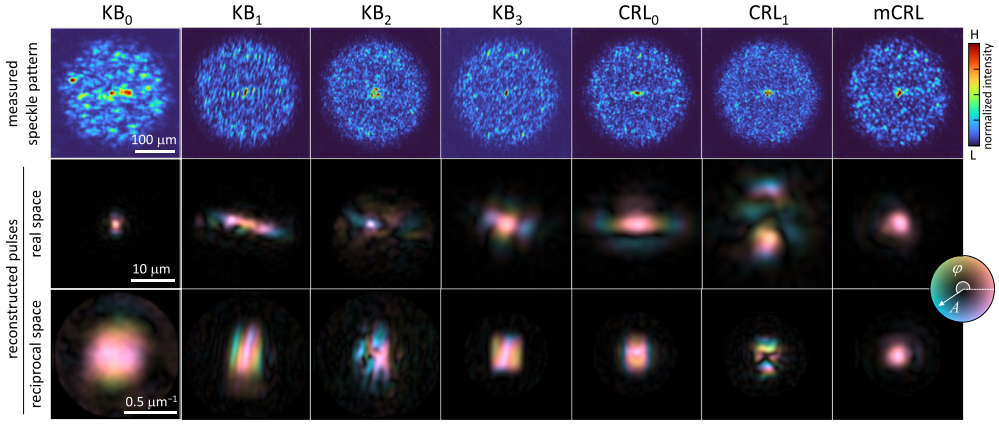

Fig. 4. Experimental field characterization results. The first row shows the raw speckle patterns independently measured in the configurations summarized in Table 1. The identifier of the configuration is displayed at the top. The second row shows the corresponding field retrieval results in real space. The third row shows the same results in reciprocal space. The lightness and hue signify the amplitude (A) and phase (φ) of retrieved fields, respectively.

The oversampling ratio (λ) of our measurements is expressed in Eq. (1) based on the space–bandwidth product (SBP) calculations (see Supplement 1):

$$\gamma = \left(1 + \frac{B_d}{B}\right)^2, \tag{1}$$

where B_d is the spatial bandwidth of the diffuser. According to Eq. (1), increasing B is inefficient in terms of oversampling and noise handling. Thus, we set B adaptively to the NA of the used focusing optics to maximize the reconstruction fidelity. Reconstruction bandwidths of 1.22 and 0.813 μm^{-1} are used for the high-NA (KB_0, KB_1, and KB_2) and low-NA (KB_3, CRL_0, CRL_1, and mCRL) configurations, respectively. Based on the Rayleigh criterion ($1.22/B$), the corresponding spatial resolutions are 1.0 and 1.5 μm, respectively.

The spatial resolution limit is also related to the oversampling ratio. Based on previous studies, $\gamma \geq 4$ is an empirically known condition for robust field reconstruction even in noiseless situations [37,43,48,50]. We found that B_d is the upper bound of achievable bandwidth ($B \leq B_d$) by applying the lower bound of γ to Eq. (1). Based on the central circular plateau of speckle patterns in Fig. 4, B_d can be estimated from the first zero of a sombrero function, $2.44/D_h$, where D_h is the hole diameter. Then, the theoretical resolution limit ($1.22/B_d$) becomes $D_h/2$, which is 150 nm in this study. Note that the practical resolution limit is greater than the theoretical value depending on experimental noise level.

D. Pulse-to-Pulse Fluctuations

Based on the SSM-based pulse characterization results, we explored the pulse-to-pulse fluctuations of PAL-XFEL. The fluctuations in pulse intensity, position, illumination angle, and shapes are analyzed for all configurations in Table 1. The results from the KB_0 configuration are shown as a representative in Fig. 5. The fluctuation results in other configurations can be found in Supplement 1. Summarized standard deviations (SDs) of fluctuations are presented in Table 2.

As denoted in Table 2, an uneven number of pulses was utilized between configurations for the fluctuation analyses. This is because we excluded the speckle patterns from the radiation-damaged diffuser before the processing steps for credibility. Accordingly, relatively smaller pulses were used for the configurations with optimized foci (KB_0 and mCRL).

The normalized pulse intensity was quantified by the intensity sum of the measured speckle pattern [Fig. 5(a)]. The measured SDs of normalized pulse energies are 0.078–0.103 and 0.51 for pink and mono beams, respectively, which is comparable to previously reported values (0.106 and 0.42) at PAL-XFEL [55].

The pulse positions and illumination angles were quantified by the center-of-intensity of retrieved pulses in real and reciprocal spaces, respectively [Figs. 5(b) and 5(c)]. Similar fluctuation results were found between configurations that share the optical setup in Fig. 3.

For the pulse positions, asymmetric fluctuation pulse positions are generally observed (Fig. S5). The KB-mirror-based configurations [Fig. 3(a); KB_0, KB_1, KB_2, and KB_3] present relatively lower fluctuations in horizontal direction (0.29–0.49 μm), while

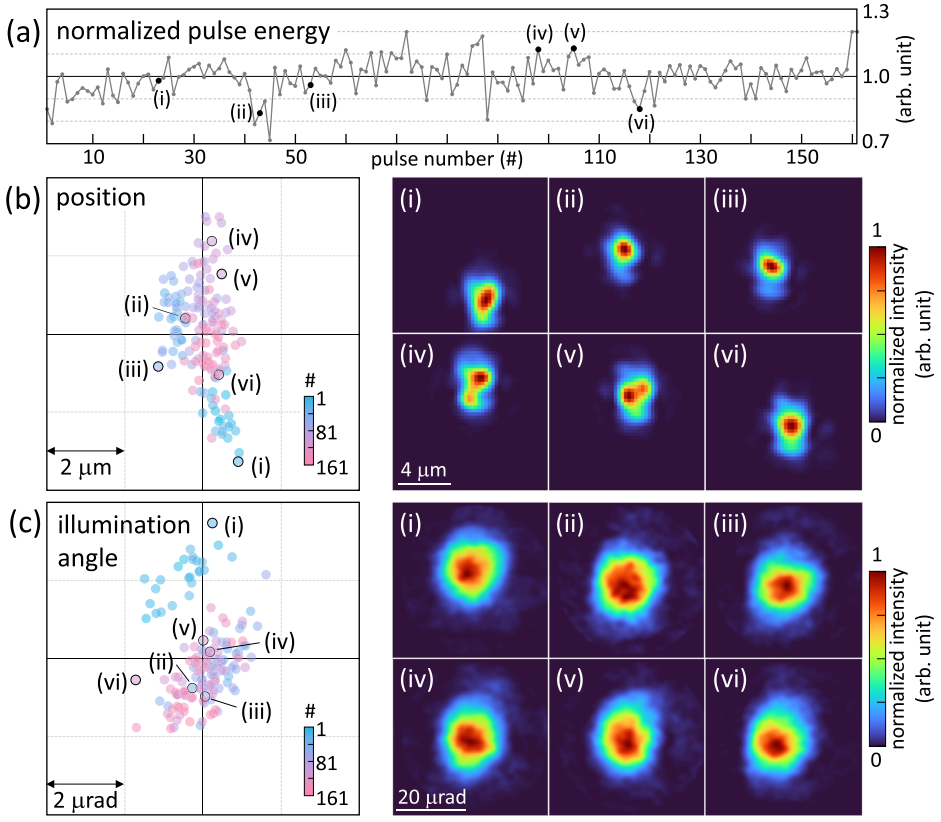

Fig. 5. Experimental pulse-to-pulse fluctuation of KB_0 configuration. (a) Pulse energy fluctuation. Pulse energies are normalized by dividing the mean value. (b) Pulse position fluctuation. (c) Pulse illumination angle fluctuation. The intensity images of six pulses (i)–(vi) are displayed in both real and reciprocal spaces. The fluctuation results in other configurations can be found in Supplement 1.

Table 2. Pulse-to-Pulse Fluctuation Results[a]

Config.	Number of Pulses	Normalized Intensity	Position (μm)		Illumination Angle (μrad)	
			Horizontal	Vertical	Horizontal	Vertical
KB_0	161	0.078	0.49	1.30	0.63	1.15
KB_1	600	0.091	0.33	0.92	0.24	0.36
KB_2	581	0.103	0.36	0.81	0.24	0.37
KB_3	499	0.082	0.29	0.80	0.33	0.12
CRL_0	1000	0.087	1.43	1.01	0.79	0.23
CRL_1	1000	0.098	0.72	1.20	0.65	0.36
mCRL	102	0.510	0.92	2.09	0.48	0.51

[a]All fluctuation values are presented in standard deviations.

similar in vertical direction (0.80–1.3 μm). The mCRL configuration presents relatively higher fluctuation in the vertical position (2.09 μm). The overall measured fluctuation level is significantly lower than the reported values (14 and 6.4 μm, respectively) at the x-ray pump probe endstation of Linac Coherent Light Source using 9 keV photons [28].

Asymmetric fluctuations are generally observed for the pulse illumination angles as well (Fig. S6). We found that fluctuations are not completely stochastic. For instance, the first 10–20 pulses in KB_0 configurations consistently show significantly higher illumination angles. Other than the sudden shift in KB_0, the KB-mirror-based configurations also present relatively lower fluctuations in horizontal direction (0.24–0.33 μrad), while similar in vertical direction (0.12–0.36 μrad). Notable reduction in vertical illumination angle fluctuation is observed for KB_3 (0.12 μrad).

To show the fluctuation on the pulse shape, the intensity images of six selected pulses in the KB_0 configuration are displayed in Fig. 5, in both real and reciprocal spaces. Significant focus shape variation is observed as shown in pulses (iv) and (v) of Fig. 5. Since the corresponding level of variations is not observed in their reciprocal space, we expect such a beam shape change is oriented from the intrinsic phase profile fluctuation of SASE pulses.

4. CONCLUSION

We proposed and demonstrated the SSM-based single-pulse characterization method for XFEL. By introducing a pulse characterization unit consisting of an aperture, a diffuser, and an imaging sensor, we successfully obtained the intensity, position, shape, and phase profile of individual SASE pulses in a single shot. The practical robustness of our method has been verified by the pulse characterization results in various experimental configurations. Such versatility is based on the general field reconstruction ability of SSM, which does not rely on *a priori* constraints or approximations. The pulse fluctuations in intensity, position, illumination angle, and shape were explored based on the pulse-to-pulse characterizations.

Though we focused on SPI in the Introduction for brevity, the precise field characterization of XFEL pulses is important in most coherence-based XFEL experiments. For instance, x-ray photon correlation spectroscopy [56–58] and x-ray speckle visibility spectroscopy [59,60] measure the far-field diffractions of samples that are actually convoluted with the reciprocal space of incident fields. Thus, the knowledge of pulse-to-pulse incident fields would help to deconvolute the incident fields from the measurements and to retrieve pure sample-induced data. We believe simultaneous incident field characterization is also possible by utilizing additional settings such as parasitic geometry [22].

We believe our method can be utilized as a standard pulse characterization tool for XFELs. Real-time pulse characterization will readily be possible with further hardware and software optimizations. It would also be advantageous for the precise alignment of optical components [21,27,61]. Further, since our field characterization method measures speckle patterns, other speckle-based pulse characterization methods may be integrable without difficulty. For instance, the transverse coherence of pulses could be characterized based on speckle visibility [55,62].

Funding. National Research Foundation of Korea (2015R1A3A2066550, 2018R1A6B4023605, 2021R1C1C2009220, 2022M3H4A1A02074314); Ministry of Trade, Industry and Energy (MOTIE) (20011661).

Disclosures. The authors declare no conflicts of interest.

Data availability. Data underlying the results presented in this paper are not publicly available at this time but may be obtained from the authors upon reasonable request.

Supplemental document. See Supplement 1 for supporting content.

REFERENCES

1. R. Barer and W. Weinstein, "A rational microscope lamp," J. R. Microsc. Soc. **73**, 148–155 (1953).
2. M. G. L. Gustafsson, "Surpassing the lateral resolution limit by a factor of two using structured illumination microscopy," J. Microsc. **198**, 82–87 (2000).
3. F. Ströhl and C. F. Kaminski, "Frontiers in structured illumination microscopy," Optica **3**, 667–677 (2016).
4. N. Streibl, "Three-dimensional imaging by a microscope," J. Opt. Soc. Am. A **2**, 121–127 (1985).
5. H. Hugonnet, M. Lee, and Y. Park, "Optimizing illumination in three-dimensional deconvolution microscopy for accurate refractive index tomography," Opt. Express **29**, 6293–6301 (2021).
6. K. A. Nugent, A. G. Peele, H. N. Chapman, and A. P. Mancuso, "Unique phase recovery for nonperiodic objects," Phys. Rev. Lett. **91**, 203902 (2003).
7. B. Abbey, K. A. Nugent, G. J. Williams, J. N. Clark, A. G. Peele, M. A. Pfeifer, M. de Jonge, and I. McNulty, "Keyhole coherent diffractive imaging," Nat. Phys. **4**, 394–398 (2008).
8. S. Takazawa, J. Kang, M. Abe, H. Uematsu, N. Ishiguro, and Y. Takahashi, "Demonstration of single-frame coherent x-ray diffraction imaging using triangular aperture: towards dynamic nanoimaging of extended objects," Opt. Express **29**, 14394–14402 (2021).
9. A. M. Maiden and J. M. Rodenburg, "An improved ptychographical phase retrieval algorithm for diffractive imaging," Ultramicroscopy **109**, 1256–1262 (2009).
10. A. Maiden, D. Johnson, and P. Li, "Further improvements to the ptychographical iterative engine," Optica **4**, 736–745 (2017).

11. C. M. Kewish, P. Thibault, M. Dierolf, O. Bunk, A. Menzel, J. Vila-Comamala, K. Jefimovs, and F. Pfeiffer, "Ptychographic characterization of the wavefield in the focus of reflective hard x-ray optics," Ultramicroscopy **110**, 325–329 (2010).
12. A. Schropp, P. Boye, J. M. Feldkamp, R. Hoppe, J. Patommel, D. Samberg, S. Stephan, K. Giewekemeyer, R. N. Wilke, T. Salditt, J. Gulden, A. P. Mancuso, I. A. Vartanyants, E. Weckert, S. Schöder, M. Burghammer, and C. G. Schroer, "Hard x-ray nanobeam characterization by coherent diffraction microscopy," Appl. Phys. Lett. **96**, 091102 (2010).
13. S. Hönig, R. Hoppe, J. Patommel, A. Schropp, S. Stephan, S. Schöder, M. Burghammer, and C. G. Schroer, "Full optical characterization of coherent x-ray nanobeams by ptychographic imaging," Opt. Express **19**, 16324–16329 (2011).
14. J. Vila-Comamala, A. Diaz, M. Guizar-Sicairos, A. Mantion, C. M. Kewish, A. Menzel, O. Bunk, and C. David, "Characterization of high-resolution diffractive x-ray optics by ptychographic coherent diffractive imaging," Opt. Express **19**, 21333–21344 (2011).
15. R. Neutze, R. Wouts, D. van der Spoel, E. Weckert, and J. Hajdu, "Potential for biomolecular imaging with femtosecond x-ray pulses," Nature **406**, 752–757 (2000).
16. H. N. Chapman, A. Barty, M. J. Bogan, *et al.*, "Femtosecond diffractive imaging with a soft-x-ray free-electron laser," Nat. Phys. **2**, 839–843 (2006).
17. M. J. Bogan, W. H. Benner, S. Boutet, U. Rohner, M. Frank, A. Barty, M. M. Seibert, F. Maia, S. Marchesini, S. Bajt, B. Woods, V. Riot, S. P. Hau-Riege, M. Svenda, E. Marklund, E. Spiller, J. Hajdu, and H. N. Chapman, "Single particle x-ray diffractive imaging," Nano Lett. **8**, 310–316 (2008).
18. M. M. Seibert, T. Ekeberg, F. R. N. C. Maia, *et al.*, "Single mimivirus particles intercepted and imaged with an x-ray laser," Nature **470**, 78–81 (2011).
19. Q. Shen, I. Bazarov, and P. Thibault, "Diffractive imaging of nonperiodic materials with future coherent x-ray sources," J. Synchrotron Radiat. **11**, 432–438 (2004).
20. Y. Kayser, S. Rutishauser, T. Katayama, T. Kameshima, H. Ohashi, U. Flechsig, M. Yabashi, and C. David, "Shot-to-shot diagnostic of the longitudinal photon source position at the SPring-8 Angstrom compact free electron laser by means of x-ray grating interferometry," Opt. Lett. **41**, 733–736 (2016).
21. M. Seaberg, R. Cojocaru, S. Berujon, *et al.*, "Wavefront sensing at x-ray free-electron lasers," J. Synchrotron Radiat. **26**, 1115–1126 (2019).
22. B. A. Pound, K. M. Mertes, A. V. Carr, M. H. Seaberg, M. S. Hunter, W. C. Ward, J. F. Hunter, C. M. Sweeney, C. M. Sewell, N. R. Weisse-Bernstein, J. K. S. Baldwin, and R. L. Sandberg, "Ptychography at the Linac coherent light source in a parasitic geometry," J. Appl. Crystallogr. **53**, 1276–1282 (2020).
23. K. Tiedtke, A. Azima, N. von Bargen, *et al.*, "The soft x-ray free-electron laser FLASH at DESY: beamlines, diagnostics and end-stations," New J. Phys. **11**, 023029 (2009).
24. A. Schropp, R. Hoppe, V. Meier, J. Patommel, F. Seiboth, H. J. Lee, B. Nagler, E. C. Galtier, B. Arnold, U. Zastrau, J. B. Hastings, D. Nilsson, F. Uhlén, U. Vogt, H. M. Hertz, and C. G. Schroer, "Full spatial characterization of a nanofocused x-ray free-electron laser beam by ptychographic imaging," Sci. Rep. **3**, 1633 (2013).
25. S. Sala, B. J. Daurer, M. Odstrcil, F. Capotondi, E. Pedersoli, M. F. Hantke, M. Manfredda, N. D. Loh, P. Thibault, and F. R. N. C. Maia, "Pulse-to-pulse wavefront sensing at free-electron lasers using ptychography," J. Appl. Crystallogr. **53**, 949–956 (2020).
26. B. J. Daurer, S. Sala, M. F. Hantke, H. K. N. Reddy, J. Bielecki, Z. Shen, C. Nettelblad, M. Svenda, T. Ekeberg, G. A. Carini, P. Hart, T. Osipov, A. Aquila, N. D. Loh, F. R. N. C. Maia, and P. Thibault, "Ptychographic wavefront characterization for single-particle imaging at x-ray lasers," Optica **8**, 551–562 (2021).
27. B. Keitel, E. Plonjes, S. Kreis, M. Kuhlmann, K. Tiedtke, T. Mey, B. Schafer, and K. Mann, "Hartmann wavefront sensors and their application at FLASH," J. Synchrotron Radiat. **23**, 43–49 (2016).
28. S. Rutishauser, L. Samoylova, J. Krzywinski, O. Bunk, J. Grünert, H. Sinn, M. Cammarata, D. M. Fritz, and C. David, "Exploring the wavefront of hard x-ray free-electron laser radiation," Nat. Commun. **3**, 947 (2012).
29. Y. Liu, M. Seaberg, D. Zhu, J. Krzywinski, F. Seiboth, C. Hardin, D. Cocco, A. Aquila, B. Nagler, H. J. Lee, S. Boutet, Y. Feng, Y. Ding, G. Marcus, and A. Sakdinawat, "High-accuracy wavefront sensing for x-ray free electron lasers," Optica **5**, 967–975 (2018).
30. S. Berujon, E. Ziegler, and P. Cloetens, "X-ray pulse wavefront metrology using speckle tracking," J. Synchrotron Radiat. **22**, 886–894 (2015).
31. F. Pfeiffer, T. Weitkamp, O. Bunk, and C. David, "Phase retrieval and differential phase-contrast imaging with low-brilliance x-ray sources," Nat. Phys. **2**, 258–261 (2006).
32. P. Bon, G. Maucort, B. Wattellier, and S. Monneret, "Quadriwave lateral shearing interferometry for quantitative phase microscopy of living cells," Opt. Express **17**, 13080–13094 (2009).
33. M. Servin, M. Cywiak, and A. Dávila, "Lateral shearing interferometry: theoretical limits with practical consequences," Opt. Express **15**, 17805–17818 (2007).
34. I. Choi, K. Lee, and Y. Park, "Compensation of aberration in quantitative phase imaging using lateral shifting and spiral phase integration," Opt. Express **25**, 30771–30779 (2017).
35. J. M. Huntley, "Noise-immune phase unwrapping algorithm," Appl. Opt. **28**, 3268–3270 (1989).
36. D. C. Ghiglia and L. A. Romero, "Minimum Lp-norm two-dimensional phase unwrapping," J. Opt. Soc. Am. A **13**, 1999–2013 (1996).
37. K. Lee and Y. Park, "Exploiting the speckle-correlation scattering matrix for a compact reference-free holographic image sensor," Nat. Commun. **7**, 13359 (2016).
38. M. Jang, Y. Horie, A. Shibukawa, J. Brake, Y. Liu, S. M. Kamali, A. Arbabi, H. Ruan, A. Faraon, and C. Yang, "Wavefront shaping with disorder-engineered metasurfaces," Nat. Photonics **12**, 84–90 (2018).
39. J. Oh, K. Lee, and Y. Park, "Single-shot reference-free holographic imaging using a liquid crystal geometric phase diffuser," Laser Photon. Rev. **16**, 2100559 (2022).
40. F. Zhang, B. Chen, G. R. Morrison, J. Vila-Comamala, M. Guizar-Sicairos, and I. K. Robinson, "Phase retrieval by coherent modulation imaging," Nat. Commun. **7**, 13367 (2016).
41. O. Katz, P. Heidmann, M. Fink, and S. Gigan, "Non-invasive single-shot imaging through scattering layers and around corners via speckle correlations," Nat. Photonics **8**, 784–790 (2014).
42. N. Antipa, G. Kuo, R. Heckel, B. Mildenhall, E. Bostan, R. Ng, and L. Waller, "DiffuserCam: lensless single-exposure 3D imaging," Optica **5**, 1–9 (2018).
43. K. Lee and Y. Park, "Interpreting intensity speckle as the coherency matrix of classical light," Phys. Rev. Appl. **12**, 024003 (2019).
44. Y. Baek, K. Lee, J. Oh, and Y. Park, "Speckle-correlation scattering matrix approaches for imaging and sensing through turbidity," Sensors **20**, 3147 (2020).
45. V. Elser and R. P. Millane, "Reconstruction of an object from its symmetry-averaged diffraction pattern," Acta Crystallogr. A **64**, 273–279 (2008).
46. T. B. Edo, D. J. Batey, A. M. Maiden, C. Rau, U. Wagner, Z. D. Pešić, T. A. Waigh, and J. M. Rodenburg, "Sampling in x-ray ptychography," Phys. Rev. A **87**, 053850 (2013).
47. J. Miao, T. Ishikawa, E. H. Anderson, and K. O. Hodgson, "Phase retrieval of diffraction patterns from noncrystalline samples using the oversampling method," Phys. Rev. B **67**, 174104 (2003).
48. G. Wang, G. B. Giannakis, and Y. C. Eldar, "Solving systems of random quadratic equations via truncated amplitude flow," IEEE Trans. Inf. Theory **64**, 773–794 (2018).
49. J. R. Fienup and C. C. Wackerman, "Phase-retrieval stagnation problems and solutions," J. Opt. Soc. Am. A **3**, 1897–1907 (1986).
50. E. J. Candès, X. Li, and M. Soltanolkotabi, "Phase retrieval via Wirtinger flow: theory and algorithms," IEEE Trans. Inf. Theory **61**, 1985–2007 (2015).
51. F. Zhang and J. M. Rodenburg, "Phase retrieval based on wave-front relay and modulation," Phys. Rev. B **82**, 121104 (2010).
52. J. Kim, H.-Y. Kim, J. Park, S. Kim, S. Kim, S. Rah, J. Lim, and K. H. Nam, "Focusing x-ray free-electron laser pulses using Kirkpatrick-Baez mirrors at the NCI hutch of the PAL-XFEL," J. Synchrotron Radiat. **25**, 289–292 (2018).

53. C. David, S. Gorelick, S. Rutishauser, J. Krzywinski, J. Vila-Comamala, V. A. Guzenko, O. Bunk, E. Färm, M. Ritala, M. Cammarata, D. M. Fritz, R. Barrett, L. Samoylova, J. Grünert, and H. Sinn, "Nanofocusing of hard x-ray free electron laser pulses using diamond based Fresnel zone plates," Sci. Rep. **1**, 57 (2011).
54. M. Makita, P. Karvinen, V. A. Guzenko, N. Kujala, P. Vagovic, and C. David, "Fabrication of diamond diffraction gratings for experiments with intense hard x-rays," Microelectron. Eng. **176**, 75–78 (2017).
55. K. Yun, S. Kim, D. Kim, M. Chung, W. Jo, H. Hwang, D. Nam, S. Kim, J. Kim, S.-Y. Park, K. S. Kim, C. Song, S. Lee, and H. Kim, "Coherence and pulse duration characterization of the PAL-XFEL in the hard x-ray regime," Sci. Rep. **9**, 3300 (2019).
56. M. H. Seaberg, B. Holladay, J. C. T. Lee, *et al.*, "Nanosecond x-ray photon correlation spectroscopy on magnetic skyrmions," Phys. Rev. Lett. **119**, 067403 (2017).
57. F. Lehmkühler, F. Dallari, A. Jain, M. Sikorski, J. Möller, L. Frenzel, I. Lokteva, G. Mills, M. Walther, H. Sinn, F. Schulz, M. Dartsch, V. Markmann, R. Bean, Y. Kim, P. Vagovic, A. Madsen, A. P. Mancuso, and G. Grübel, "Emergence of anomalous dynamics in soft matter probed at the European XFEL," Proc. Natl. Acad. Sci. USA **117**, 24110–24116 (2020).
58. F. Lehmkühler, W. Roseker, and G. Grübel, "From femtoseconds to hours—measuring dynamics over 18 orders of magnitude with coherent x-rays," Appl. Sci. **11**, 6179 (2021).
59. F. Perakis, G. Camisasca, T. J. Lane, *et al.*, "Coherent x-rays reveal the influence of cage effects on ultrafast water dynamics," Nat. Commun. **9**, 1917 (2018).
60. Y. Sun, G. Carini, M. Chollet, F.-J. Decker, M. Dunne, P. Fuoss, S. O. Hruszkewycz, T. J. Lane, K. Nakahara, S. Nelson, A. Robert, T. Sato, S. Song, G. B. Stephenson, M. Sutton, T. B. Van Driel, C. Weninger, and D. Zhu, "Nonuniform flow dynamics probed by nanosecond x-ray speckle visibility spectroscopy," Phys. Rev. Lett. **127**, 058001 (2021).
61. M. Kahnt, S. Kalbfleisch, A. Björling, E. Malm, L. Pickworth, and U. Johansson, "Complete alignment of a KB-mirror system guided by ptychography," Opt. Express **30**, 42308–42322 (2022).
62. F. Lehmkühler, C. Gutt, B. Fischer, M. A. Schroer, M. Sikorski, S. Song, W. Roseker, J. Glownia, M. Chollet, S. Nelson, K. Tono, T. Katayama, M. Yabashi, T. Ishikawa, A. Robert, and G. Grübel, "Single shot coherence properties of the free-electron laser SACLA in the hard x-ray regime," Sci. Rep. **4**, 5234 (2014).

143.248.11.147 (ts 2023-04-07 03:15:56)